

## **Author Manuscript**

**Title:** Rhodium Single-Atom Catalysts on Titania for Reverse Water Gas Shift Reaction Explored by First Principles Mechanistic Analysis and Compared to Nanoclusters

**Authors:** Francis Doherty; Bryan R. Goldsmith

This is the author manuscript accepted for publication. It has not been through the copyediting, typesetting, pagination and proofreading process, which may lead to differences between this version and the Version of Record.

**To be cited as:** 10.1002/cctc.202100292

**Link to VoR:** <https://doi.org/10.1002/cctc.202100292>

# Rhodium Single-Atom Catalysts on Titania for Reverse Water Gas Shift Reaction Explored by First Principles Mechanistic Analysis and Compared to Nanoclusters

Francis Doherty and Prof. Bryan R. Goldsmith\*

*Department of Chemical Engineering, University of Michigan, 2300 Hayward St., Ann Arbor, MI 48109-2136, USA*

*Catalysis Science and Technology Institute, University of Michigan, 2300 Hayward St., Ann Arbor, MI 48109-2136, USA*

*\*email: bgoldsm@umich.edu; Twitter: @BryanRGoldsmith*

**ABSTRACT:** The thermocatalytic reduction of CO<sub>2</sub> by H<sub>2</sub> often proceeds via two competing reaction mechanisms—the reverse water gas shift reaction (rWGSR, CO<sub>2</sub> + H<sub>2</sub> ⇌ CO + H<sub>2</sub>O) and methanation (CO<sub>2</sub> + 4H<sub>2</sub> ⇌ CH<sub>4</sub> + 2H<sub>2</sub>O). Atomically dispersed Rh<sub>1</sub> catalysts on TiO<sub>2</sub> show high selectivity toward the rWGSR compared with larger Rh nanoclusters, but the origin of this size-dependent selectivity has not been fully explained. Here we report density functional theory (DFT) calculations and microkinetic simulations that clarify the Rh<sub>1</sub> active sites and rWGSR pathway on anatase TiO<sub>2</sub>(101), as well as the high rWGSR selectivity of Rh<sub>1</sub> compared with supported Rh<sub>x</sub> (x = 2–8 atoms) nanoclusters. DFT-computed formation energies, vibrational frequency analysis, and microkinetic modeling suggest three plausible active sites: Rh<sub>1</sub> on titania (Rh<sub>1</sub>/TiO<sub>2</sub>(101)), Rh<sub>1</sub> with a nearby hydroxyl group (Rh<sub>1</sub>OH/TiO<sub>2</sub>(101)), and Rh<sub>1</sub> near an oxygen vacancy at a three-fold coordinated site (Rh<sub>1</sub> near O<sub>3c</sub>vac). Predicted turnover frequencies and apparent activation barriers for Rh<sub>1</sub> indicate a faster reaction involving CO<sub>2</sub> dissociation assisted by a support oxygen vacancy via Rh<sub>1</sub> near O<sub>3c</sub>vac, as well as slower reactions involving Rh<sub>1</sub>OH/TiO<sub>2</sub>(101) or Rh<sub>1</sub>/TiO<sub>2</sub>(101) through a COOH intermediate. These Rh<sub>1</sub> sites are selective toward CO rather than CH<sub>4</sub> because of the weak adsorption of CO, large barrier for C-O bond dissociation, and the lack of nearby metal sites for H<sub>2</sub> dissociation, in contrast to Rh<sub>x</sub> nanoclusters, including Rh<sub>2</sub> dimers.

## INTRODUCTION

The size of supported nanoparticles affects catalytic performance for many reactions, such as CO oxidation,<sup>[1]</sup> methane activation,<sup>[2]</sup> and CO<sub>2</sub> reduction.<sup>[3,4]</sup> Taking this size-dependent catalytic phenomenon to the limit, researchers have been developing atomically dispersed (i.e., single atom) catalysts, which frequently show modified activity and selectivity relative to their larger nanocluster (< 2 nm) or nanoparticle counterparts.<sup>[5–8]</sup> Importantly, atomically dispersed catalysts can also achieve the maximum possible dispersion of metal on a support, making optimal use of rare and expensive metals.

In some cases, atomically dispersed catalysts are more active or selective than nanoclusters. For example, the direct conversion of methane to methanol was achieved with high selectivity by using atomically dispersed rhodium supported on titanium dioxide (Rh<sub>1</sub>/TiO<sub>2</sub>).<sup>[9]</sup> In other cases, nanoclusters display higher activity than atomically dispersed catalysts (e.g., Pt/CeO<sub>2</sub> for low-

temperature CO oxidation).<sup>[10]</sup> Nevertheless, the activity and selectivity differences between nanoclusters and their atomically dispersed counterparts are not well-understood for many reactions.<sup>[11]</sup>

One reaction where atomically dispersed catalysts and their corresponding nanoclusters have shown different activity and selectivity is the thermocatalytic reduction of CO<sub>2</sub> by H<sub>2</sub>, which has become an intensively studied area of research because of environmental concerns.<sup>[12,13]</sup> Thermocatalytic CO<sub>2</sub> reduction can occur via the reverse water gas shift reaction (rWGSR, CO<sub>2</sub> + H<sub>2</sub> ⇌ CO + H<sub>2</sub>O) or catalytic methanation (CO<sub>2</sub> + 4H<sub>2</sub> ⇌ CH<sub>4</sub> + 2H<sub>2</sub>O) depending on the reaction conditions and catalyst. Methanol synthesis from the hydrogenation of CO<sub>2</sub> is also an important reaction for improving the chemical industry's environmental impact,<sup>[11]</sup> but is hindered by the competing rWGSR.

Notably, the activity and selectivity of CO<sub>2</sub> reduction to products such as methane and CO

depends strongly on the metal catalyst size.<sup>[4,14,15]</sup> In particular, CO<sub>2</sub> reduction by Rh/TiO<sub>2</sub> displays a strong selectivity dependence between CO vs. CH<sub>4</sub> on the fraction of atomically dispersed Rh<sub>1</sub> relative to Rh nanoclusters. Correlations were observed between catalytic methanation turnover frequency (TOF) and the fraction of Rh nanoclusters, and between the TOF of the rWGSR and the fraction of Rh<sub>1</sub> species.<sup>[3]</sup> These Rh<sub>1</sub> species can be synthesized via techniques such as strong electrostatic adsorption<sup>[16–18]</sup> and atomic layer deposition,<sup>[19,20]</sup> or can spontaneously form via Rh nanocluster disintegration under reaction conditions.<sup>[21–27]</sup> The Rh<sub>1</sub> species are typically detected as gem-dicarbonyl Rh<sub>1</sub>(CO)<sub>2</sub> complexes via diffuse reflectance Fourier transform infrared spectroscopy (DRIFTS)<sup>[3,28]</sup> and may anchor on the surface oxygen or in oxygen vacancies on metal oxide supports.<sup>[29–32]</sup> Stable Rh<sub>1</sub> species coexist with Rh particles on TiO<sub>2</sub> with ratios that depend on the loading percent of Rh, temperature, and gas composition.

The large difference in selectivity between Rh<sub>1</sub> species and Rh nanoclusters toward the rWGSR is not well-understood at the atomic level, in part due to a lack of knowledge of the precise active sites and elementary reaction steps. Several rWGSR mechanisms for Rh<sub>1</sub> on vacancy-free anatase TiO<sub>2</sub>(101) were explored based on electronic energies predicted using density functional theory (DFT) modeling.<sup>[33]</sup> The high selectivity of Rh<sub>1</sub> toward CO was proposed to arise from a lack of orbital overlap between the highest occupied molecular orbital of Rh<sub>1</sub> and the lowest unoccupied molecular orbital of H<sub>2</sub>, which prevents H<sub>2</sub> adsorption on Rh<sub>1</sub> while CO is bound and halts the reaction before hydrogenation to CH<sub>4</sub>.<sup>[33]</sup> However, the predicted rWGSR mechanism includes a large activation barrier of 1.9 eV for the second elementary hydrogenation step to form the CO and H<sub>2</sub>O from the commonly proposed carboxyl (\*COOH) intermediate.<sup>[34,35]</sup> Ir<sub>1</sub>/FeO<sub>x</sub>, Ru<sub>1</sub>/Al<sub>2</sub>O<sub>3</sub>, and Pt<sub>1</sub>/FeO<sub>x</sub> have similar TOFs as Rh<sub>1</sub>/TiO<sub>2</sub> for CO<sub>2</sub> reduction (i.e., TOF of 0.005–0.03 s<sup>-1</sup> at 473 K),<sup>[3]</sup> with measured apparent activation energies around 0.52–0.82 eV between 270–350 K,<sup>[36,37]</sup> suggesting alternative reaction pathways or different Rh<sub>1</sub> catalytic sites may be responsible for the observed activity and selectivity differences compared with Rh nanoclusters. Further atomistic

modeling of the rWGSR on Rh<sub>1</sub>/TiO<sub>2</sub> and Rh nanoclusters would clarify the origin for the rWGSR activity and selectivity differences with particle size.

Here we report first-principles modeling studies of Rh<sub>1</sub> sites and small Rh<sub>x</sub> nanoclusters ( $x = 2–8$ ) on anatase TiO<sub>2</sub> to understand the activity of Rh<sub>1</sub> sites toward rWGSR and to explain the high selectivity of Rh<sub>1</sub> toward rWGSR compared to nanoclusters. Plausible Rh<sub>1</sub> active sites on anatase TiO<sub>2</sub> for rWGSR are identified based on DFT-predicted formation energies, gem-dicarbonyl vibrational frequency analysis, and microkinetic modeling. Rh<sub>1</sub> near an oxygen vacancy at a three-fold coordinated site (Rh<sub>1</sub> near O<sub>3c</sub>vac) is predicted to be the most active Rh<sub>1</sub> site because the nearby oxygen vacancy helps activate CO<sub>2</sub>, yielding faster kinetics than proceeding through a \*COOH intermediate. Rh<sub>1</sub> species on TiO<sub>2</sub> are found to be more selective toward rWGSR than Rh<sub>x</sub>/TiO<sub>2</sub> nanoclusters because (i) CO adsorbs weaker to Rh and has a stronger C–O bond strength on all Rh<sub>1</sub> sites compared with nanoclusters, and (ii) Rh<sub>1</sub> active sites have a higher barrier for H<sub>2</sub> dissociation and adsorb hydrogen weaker than nanoclusters. The Rh<sub>1</sub> sites are predicted to be unique in their ability to have high selectivity toward CO even compared to Rh<sub>2</sub> dimers.

## COMPUTATIONAL METHODS

*DFT calculations.* All DFT calculations were conducted using the Vienna Ab initio Simulation Package.<sup>[38–40]</sup> Electron-ion interactions were treated with the projector augmented-wave method.<sup>[41]</sup> Anatase TiO<sub>2</sub>(101) was studied because the anatase phase is more stable than rutile for high-surface area particles smaller than ~14 nm.<sup>[42,43]</sup> The (101) surface was selected because it is the most abundant facet of the anatase surface.<sup>[44]</sup> A five-layer thick anatase TiO<sub>2</sub>(101) slab (1×3 surface, 174 atoms total) with a 20 Å vacuum layer was built in the Atomic Simulation Environment (ASE).<sup>[45]</sup> Bulk experimental lattice constants of 3.78 Å ( $a$ ,  $b$ ) and 9.51 Å ( $c$ ) were specified for the TiO<sub>2</sub>(101) model.<sup>[46]</sup> The bottom two layers of the TiO<sub>2</sub>(101) slab were fixed in the position of the bulk lattice, whereas the top three layers could relax during geometry optimization. The (134) surface, which exhibits (100)-like facets between steps, was chosen as a step-edge model. The (134) model was constructed as a 1×3 periodic surface slab that was

three layers thick (192 atoms total). The top two layers of the (134) slab could relax during geometry optimization. Dipole corrections were included in the  $z$  direction for each model surface. A plane wave basis set with a cutoff energy of 340 eV was selected after benchmarking. The  $k$ -space was sampled using a  $4 \times 4 \times 1$  Monkhorst-Pack grid. Transition states were found using the Climbing Image Nudged Elastic Band method.<sup>[47]</sup>

The PBE+U functional with the D3 dispersion<sup>[48]</sup> correction was used for all calculations.<sup>[49,50]</sup> DFT using only PBE fails to describe the strong on-site Coulomb interaction of localized  $d$ -electrons in  $\text{TiO}_2$ , so a  $U$  value of 2.5 eV was chosen to reproduce the reaction energy of O vacancy formation in  $\text{TiO}_2$ ,<sup>[50]</sup> which is important for the catalytic systems studied here.

Formation energies and binding energies were calculated using:

$$\Delta E_f = E_{\text{ads/Rh/TiO}_2} - (E_{\text{TiO}_2} + E_{\text{bulk}} + E_{\text{mol}(g)})$$

$$\Delta E_b = E_{\text{ads/Rh/TiO}_2} - (E_{\text{Rh/TiO}_2} + E_{\text{mol}(g)})$$

Here  $\Delta E_f$  is the formation energy of a single-atom-adsorbate complex (e.g.,  $\text{Rh}_1(\text{CO})_2/\text{TiO}_2$ ),  $E_{\text{ads/Rh/TiO}_2}$  is the DFT-calculated electronic energy of the single-atom-adsorbate complex,  $E_{\text{TiO}_2}$  is the energy of the  $\text{TiO}_2$  surface (including an O vacancy, Ti vacancy, or OH group if present),  $E_{\text{bulk}}$  is the per-atom energy of Rh in the bulk face-centered cubic crystal,  $E_{\text{mol}(g)}$  is the energy of the adsorbate molecule(s) in the gas phase,  $\Delta E_b$  is the binding energy of an adsorbate to  $\text{Rh}_x/\text{TiO}_2$ , and  $E_{\text{Rh/TiO}_2}$  is the energy of the  $\text{Rh}_x/\text{TiO}_2$  system itself. The bulk Rh was constructed using the optimized lattice constant of 3.816 Å ( $a, b, c$ ).

The strength of the C-O bond for adsorbed CO was calculated as:

$$E_{\text{C-O}} = (E_{\text{Rh-CO}} + E_{\text{H}_2(g)}) - (E_{\text{Rh-C}} + E_{\text{H}_2\text{O}(g)})$$

where  $E_{\text{C-O}}$  is the C-O bond energy,  $E_{\text{Rh-CO}}$  is the binding energy of CO on the supported Rh species,  $E_{\text{Rh-C}}$  is the binding energy of atomic C on Rh, and  $E_{\text{H}_2(g)}$  and  $E_{\text{H}_2\text{O}(g)}$  are the gas-phase electronic energies of hydrogen and water. Using this formula, the energy difference between bound CO and dissociated C and O is found, resulting in the C-O bond strength.  $\text{H}_2$  and  $\text{H}_2\text{O}$  are chosen as the gas phase reference states for removing O from CO, since the reaction occurs under reducing conditions with plentiful  $\text{H}_2(g)$ .

Reported Gibbs free energies ( $\Delta G$ ) used in free energy diagrams and microkinetic modeling include ideal-gas corrections for molecular rotations, translations, and vibrations, as well as hindered rotation and vibration of the adsorbed species (as implemented in the ASE package).

Vibrational frequencies for Gibbs free energy calculations and for comparison with DRIFTS were computed within the harmonic approximation. The gas phase CO vibrational frequency calculated using PBE was  $2103 \text{ cm}^{-1}$ , which is about  $40 \text{ cm}^{-1}$  lower than the experimentally measured value of  $2143 \text{ cm}^{-1}$ .<sup>[51]</sup> For comparison with experimental DRIFTS measurements, a  $40 \text{ cm}^{-1}$  rigid shift was applied to all calculated vibrational frequencies for adsorbed CO to correct for this difference. Further modeling details are provided in the Supporting Information (SI).

*Nanocluster geometry search.* A genetic algorithm (GA) was used to search the structure of supported  $\text{Rh}_x$  nanoclusters ( $x = 4-8$  atoms) on anatase  $\text{TiO}_2(101)$ . The GA is based on an implementation in ASE.<sup>[52,53]</sup> The positions and structures of  $\text{Rh}_1$ ,  $\text{Rh}_2$ , and  $\text{Rh}_3$  on  $\text{TiO}_2(101)$  were manually searched.

For each GA search, the starting population contained 12 randomly generated  $\text{Rh}_x$  structures. Next, DFT calculations were performed to evaluate the total electronic energy of each  $\text{Rh}_x$  structure in the population. All the atoms in  $\text{Rh}_x$  nanoclusters were relaxed during GA calculations, but a one-layer  $\text{TiO}_2(101)$  support was fixed during the GA algorithm. Mutation and cross-over operations were applied to existing structures in the population to generate new structures.<sup>[52]</sup> The calculated total electronic energy was used to evaluate the fitness of each structure. The above steps were repeated to optimize the population of candidate nanoclusters. The GA was terminated if no new low-energy structures were found within 1000 attempts or after 80 generations, whichever came first. Repeated runs of the GA with different initial populations reidentified the same ground-state structures of the  $\text{Rh}_x$  nanoclusters. Final structures were re-optimized on a full 6-layer  $\text{TiO}_2$  slab (changes in each cluster structure were minimal upon re-optimization). More details on the GA workflow are discussed in the SI and shown in **Fig. S1**.

*Microkinetic simulations.* First-principles mean-field microkinetic simulations<sup>[54]</sup> of the rWGSR

were conducted to predict TOFs, apparent activation barriers, and the degree of rate control (DRC)<sup>[55]</sup> for plausible Rh<sub>1</sub>/TiO<sub>2</sub> sites and reaction mechanisms. All microkinetic simulations used the MKMCXX code.<sup>[56]</sup> The DFT-based microkinetic simulation approach that we use has been presented in detail elsewhere,<sup>[56,57]</sup> so here we summarize only the main points. The DFT-calculated forward and backward activation energies were used to calculate the rate constant of each elementary step. For surface reactions, the rate constant of step *i* was calculated using the Arrhenius equation. Differential equations for all the reaction species were built using the predicted rate and equilibrium constants and the set of elementary steps. The rates of the elementary steps were computed based on the steady-state coverages. Steady-state surface coverages were determined by integrating the differential equations in time until changes in the surface coverages were less than 10<sup>-8</sup>. In our simulations, the gas phase consisted of CO<sub>2</sub> and H<sub>2</sub> in a 1:4 molar ratio at a total pressure of 1 atm, within the range of typical experimental reaction conditions.<sup>[58]</sup> Further microkinetic modeling details including the elementary steps of each studied rWGS mechanism are provided in the SI.

## RESULTS AND DISCUSSION

### Atomically dispersed Rh<sub>1</sub> catalysts for rWGS

*Rh<sub>1</sub> binding locations on TiO<sub>2</sub>.* The feasible Rh<sub>1</sub> binding locations must first be known to understand the activity and selectivity of Rh<sub>1</sub>/TiO<sub>2</sub> toward the rWGS. Atomically dispersed Rh<sub>1</sub> is known to change its coordination environment on anatase and rutile TiO<sub>2</sub> depending on the reaction conditions.<sup>[32,59]</sup> A recent study identified plausible sites for Rh<sub>1</sub> binding on anatase TiO<sub>2</sub>(101) under CO + H<sub>2</sub> reducing conditions using DFT and Fourier-transform infrared spectroscopy (FTIR), specifically Rh<sub>1</sub>(CO)<sub>2</sub> bound to two, two-fold

coordinated oxygen atoms (O<sub>2c</sub>) with and without a nearby Ti-OH group.<sup>[32]</sup> Herein we build on this prior work and expand the set of structures considered as plausible Rh<sub>1</sub>/TiO<sub>2</sub> sites, including anatase surfaces with oxygen vacancies and stepped sites.

We identify plausible binding locations for Rh<sub>1</sub> on anatase TiO<sub>2</sub> at zero Kelvin under vacuum based on DFT-computed formation energies and gem-dicarbonyl vibrational frequency analysis. The systems considered were: Rh<sub>1</sub> on clean TiO<sub>2</sub>(101), Rh<sub>1</sub> on the TiO<sub>2</sub>(134) step edge, Rh<sub>1</sub> occupying O vacancies at the two-fold coordinated (@O<sub>2c</sub>vac) and three-fold coordinated (@O<sub>3c</sub>vac) sites, Rh<sub>1</sub> occupying a Ti vacancy at the five-fold coordinated site (@Ti<sub>5c</sub>vac), and Rh<sub>1</sub> with O vacancies nearby and far away. Rh<sub>1</sub> with a nearby hydroxyl group on TiO<sub>2</sub> [Rh<sub>1</sub>OH/TiO<sub>2</sub>(101)] as proposed by Asokan *et al.*<sup>[32]</sup> is also considered.

The bare Rh<sub>1</sub> systems considered are shown in the SI (**Fig. S2**), which all have highly endothermic formation energies. In the presence of CO, the gem-dicarbonyl Rh<sub>1</sub>(CO)<sub>2</sub> complexes (**Fig. 1**) are much more stable than bare Rh<sub>1</sub> species. The Rh<sub>1</sub>(CO)<sub>2</sub> are readily detected via DRIFTS to probe the Rh<sub>1</sub> site environments and thus are considered in detail for stability and vibrational frequency analysis.<sup>[60-64]</sup>

The Rh<sub>1</sub>(CO)<sub>2</sub> formation energy on a defect-free TiO<sub>2</sub>(101) surface, where Rh<sub>1</sub> is bound through two surface oxygens (**Fig. 1a**) is exothermic (-1.80 eV). This Rh<sub>1</sub>(CO)<sub>2</sub>/TiO<sub>2</sub> complex is the same structure as that suggested in recent work based on DRIFTS, temperature programmed desorption, and DFT.<sup>[32]</sup> Experimentally, the Rh<sub>1</sub>(CO)<sub>2</sub> structure exhibits two peaks around 2097 and 2028 cm<sup>-1</sup>, being the symmetric and asymmetric C-O bond stretches, respectively.<sup>[3,65]</sup> Vibrational stretches of 2080 cm<sup>-1</sup> and 2027 cm<sup>-1</sup> for Rh<sub>1</sub>(CO)<sub>2</sub> on TiO<sub>2</sub>(101) (**Fig. 2**) are predicted, similar to experiment and prior DFT vibrational frequency assignment.<sup>[32]</sup>



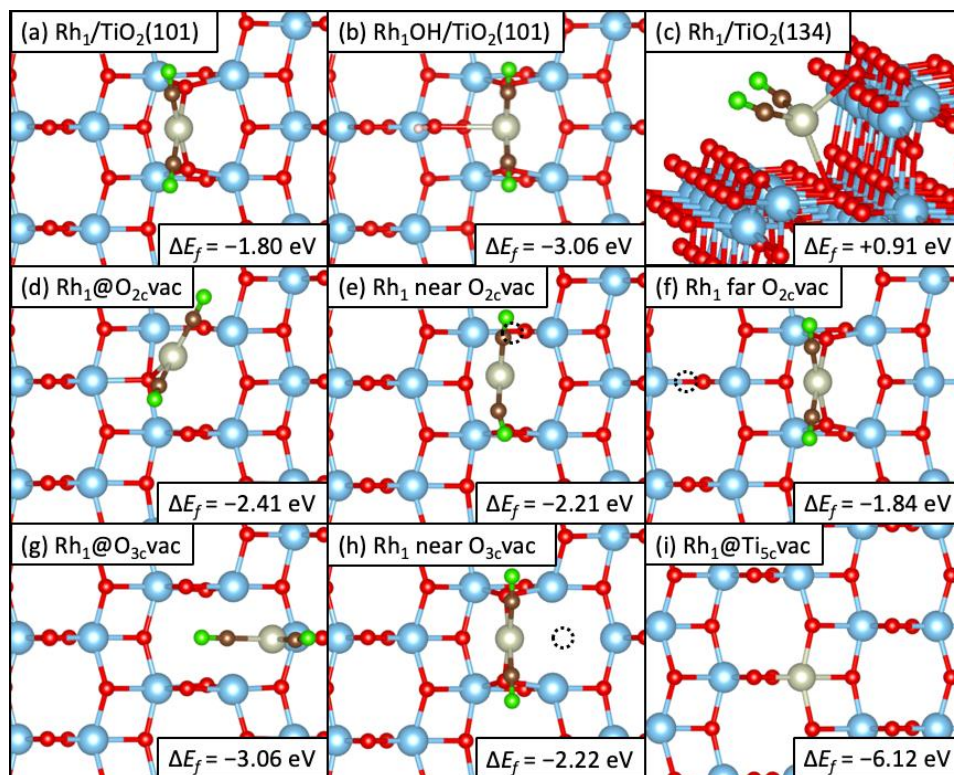


**Fig. 1.** Top view of the gem-dicarbonyl  $\text{Rh}_1(\text{CO})_2$  binding locations on anatase  $\text{TiO}_2$ , along with their formation energy ( $\Delta E_f$ ) relative to a bare  $\text{TiO}_2$  surface (defect-free, defective, or step, as relevant), Rh bulk lattice, and gaseous CO. The systems considered were: (a)  $\text{Rh}_1$  on  $\text{TiO}_2(101)$ , (b)  $\text{Rh}_1$  on  $\text{TiO}_2(101)$  with a nearby hydroxyl group, (c)  $\text{Rh}_1$  on the  $\text{TiO}_2(134)$  step edge, (d)  $\text{Rh}_1$  occupying an O vacancy at the two-fold coordinated site ( $@\text{O}_{2c}\text{vac}$ ) on  $\text{TiO}_2(101)$ , (e)  $\text{Rh}_1$  with an  $\text{O}_{2c}\text{vac}$  nearby on  $\text{TiO}_2(101)$ , (f)  $\text{Rh}_1$  with an  $\text{O}_{2c}\text{vac}$  far away on  $\text{TiO}_2(101)$ , (g)  $\text{Rh}_1$  occupying an O vacancy at the three-fold coordinated site ( $@\text{O}_{3c}\text{vac}$ ) on  $\text{TiO}_2(101)$ , (h)  $\text{Rh}_1$  near a  $\text{O}_{3c}\text{vac}$  on  $\text{TiO}_2(101)$  and (i)  $\text{Rh}_1$  in a Ti vacancy at the five-fold coordinated site ( $@\text{Ti}_{5c}\text{vac}$ ) on  $\text{TiO}_2(101)$ . Oxygen vacancies are denoted with dashed circles. Atom color legend: Blue = Ti, Red = O, Gray = Rh, Green = O in CO, Brown = C.

When considering a  $\text{TiO}_2$  surface with nearby hydroxyl group ( $\text{Rh}_1\text{OH}$ ), the  $\text{Rh}_1$  binding location does not change from the clean surface (**Fig. 1b**). The formation energy is also very exothermic ( $-3.06$  eV). The calculated vibrational frequencies of  $2093\text{ cm}^{-1}$  and  $2026\text{ cm}^{-1}$  match closely with experimental values (**Fig. 2**), differing only by  $4\text{ cm}^{-1}$  and  $1\text{ cm}^{-1}$ , respectively. These vibrational frequency predictions agree well with the prior study by Asokan *et al.*<sup>[32]</sup>

In contrast, the formation energy of the  $\text{Rh}_1(\text{CO})_2/\text{TiO}_2(134)$  step edge is highly endothermic ( $0.91$  eV, **Fig. 1c**). Besides having an endothermic formation energy,  $\text{Rh}_1(\text{CO})_2/\text{TiO}_2(134)$  was also ruled out as an abundant surface species by incompatible vibrational frequencies compared with experiment (**Fig. 2**), namely  $1973$  and  $1941\text{ cm}^{-1}$ .

Examining the effect of oxygen vacancies on the  $\text{Rh}_1/\text{TiO}_2$  system is important because they may participate in activating  $\text{CO}_2$  for the rWGSr.<sup>[64,66,67]</sup> An oxygen vacancy would allow for an alternative mechanism for  $\text{CO}_2$  dissociation into  $^*\text{CO}$  and  $^*\text{O}$  to heal the vacancy, bypassing any  $^*\text{COOH}$  intermediate. Subsurface oxygen vacancies were measured by scanning tunneling microscopy in anatase  $\text{TiO}_2$  under reducing conditions similar to those used for  $\text{CO}_2$  reduction.<sup>[68,69]</sup> Supported  $\text{Rh}_1$  has been shown via temperature programmed reduction to promote the formation of O vacancies within a P25  $\text{TiO}_2$  support, which is approximately 75% anatase and 25% rutile.<sup>[70]</sup> For (101) anatase, O vacancies were predicted by DFT to preferentially exist in the subsurface.<sup>[69,71]</sup> However, these O vacancies may diffuse throughout the lattice under reaction conditions.<sup>[71,72]</sup> Because of the mobility of O vacancies, both  $\text{O}_{2c}\text{vac}$  (**Figs. 1d-f**) and  $\text{O}_{3c}\text{vac}$

(Figs. 1g,h) surface vacancies are considered. The  $\text{Rh}_1$  inside Ti vacancies (Fig. 1i) likely have low abundance in the strong reducing environment of rWGSR. Further, the formation energy is strongly negative for  $\text{Rh}_1$  filling Ti vacancies, and they are not predicted to form  $\text{Rh}_1$ -dicarbonyl complexes because of their saturated coordination environment;<sup>[32,59]</sup> thus we do not consider Ti vacancies further as active  $\text{Rh}_1$  sites.

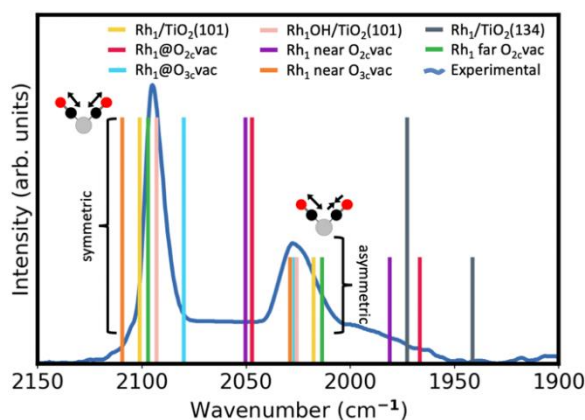


**Fig. 2.** Experimental DRIFTS spectroscopy and DFT-predicted CO stretching frequencies under the harmonic approximation for  $\text{Rh}_1(\text{CO})_2$  systems. The two peaks observed are for symmetric (high intensity peak) and asymmetric (low intensity peak) stretches of CO. Note, only the peak positions as computed by DFT are reported and the intensities are arbitrarily specified for clarity. The experimental DRIFTS spectra (300 K, 10% CO/90% Ar) is reproduced from Ref. 3. The experimental DRIFTS used P25, which is a mixture of 75% anatase and 25% rutile  $\text{TiO}_2$ .

The data in Fig. 2 shows calculated IR stretching frequencies for each considered  $\text{Rh}_1(\text{CO})_2/\text{TiO}_2$  system compared with experimental DRIFTS from Matsubu *et al.*<sup>[3]</sup>  $\text{Rh}_1@O_{2c}\text{vac}$  or near an  $O_{2c}\text{vac}$ , and the  $\text{Rh}_1/\text{TiO}_2(134)$  step edge all have frequencies far from experimentally observed values, and thus may not be present in appreciable abundance. Remaining plausible binding locations based on  $\text{Rh}_1(\text{CO})_2$  formation energies and vibrational frequency analysis are  $\text{Rh}_1@O_{3c}\text{vac}$ ,  $\text{Rh}_1$  near  $O_{3c}\text{vac}$ ,  $\text{Rh}_1/\text{TiO}_2$ , and  $\text{Rh}_1\text{OH}/\text{TiO}_2$ . In

particular, the  $\text{Rh}_1\text{OH}$  system agrees most closely with experiment, differing by less than 0.2% for both symmetric and asymmetric stretches. The  $\text{Rh}_1/\text{TiO}_2(101)$  and  $\text{Rh}_1\text{OH}/\text{TiO}_2(101)$  structures have been proposed previously as stable adsorption sites and potential active sites on anatase  $\text{TiO}_2$ ,<sup>[32,33]</sup> but  $\text{Rh}_1$  near  $O_{3c}\text{vac}$  and  $\text{Rh}_1@O_{3c}\text{vac}$  have not been studied in detail. In addition, with the exception of  $\text{Rh}_1/\text{TiO}_2(101)$ ,<sup>[33]</sup> none of these species have had their rWGSR mechanism modeled via first-principles microkinetic modeling. We note that although CO-DRIFTS probes  $\text{Rh}_1$  sites accessible by CO, which may be active sites for  $\text{CO}_2$  reduction, it is possible that these sites are not fully representative of the distribution of sites present in  $\text{CO}_2 + \text{H}_2$  reaction conditions.

*Microkinetic modeling of rWGSR on plausible  $\text{Rh}_1/\text{TiO}_2$  active sites.* Based on having exothermic gem-dicarbonyl formation energies and qualitative agreement with prior experimental CO-DRIFTS peak assignments, the  $\text{Rh}_1/\text{TiO}_2(101)$ ,  $\text{Rh}_1\text{OH}/\text{TiO}_2(101)$ ,  $\text{Rh}_1@O_{3c}\text{vac}$ , and  $\text{Rh}_1$  near  $O_{3c}\text{vac}$  are plausible active sites for rWGSR. However, we do not consider  $\text{Rh}_1@O_{3c}\text{vac}$  further because  $\text{CO}_2$  is weakly bound by this site, and the barrier for  $\text{CO}_2$  dissociation is computed to be large (1.30 eV) compared to  $\text{Rh}_1$  near  $O_{3c}\text{vac}$  (0.21 eV). To clarify the activity differences among the remaining single-atom species, DFT-based microkinetic modeling of the rWGSR reaction mechanism is performed.

$\text{CO}_2$  hydrogenation to CO can proceed through a carboxyl intermediate ( $^*\text{COOH}$ ), which further reacts with  $^*\text{H}$  to form water and CO. Alternatively, the  $^*\text{CO}_2$  can dissociate directly into  $^*\text{CO}$  and  $^*\text{O}$  by C-O bond cleavage, especially when  $^*\text{O}$  is healing an oxygen vacancy on reducible supports such as  $\text{CeO}_2$  and  $\text{TiO}_2$ .<sup>[58,73]</sup> In either case,  $^*\text{CO}$  will desorb if not allowed to react further. The selectivity will depend on the binding strength of CO and the availability of nearby  $^*\text{H}$ , both of which vary between  $\text{Rh}_1$  and  $\text{Rh}_x$ .

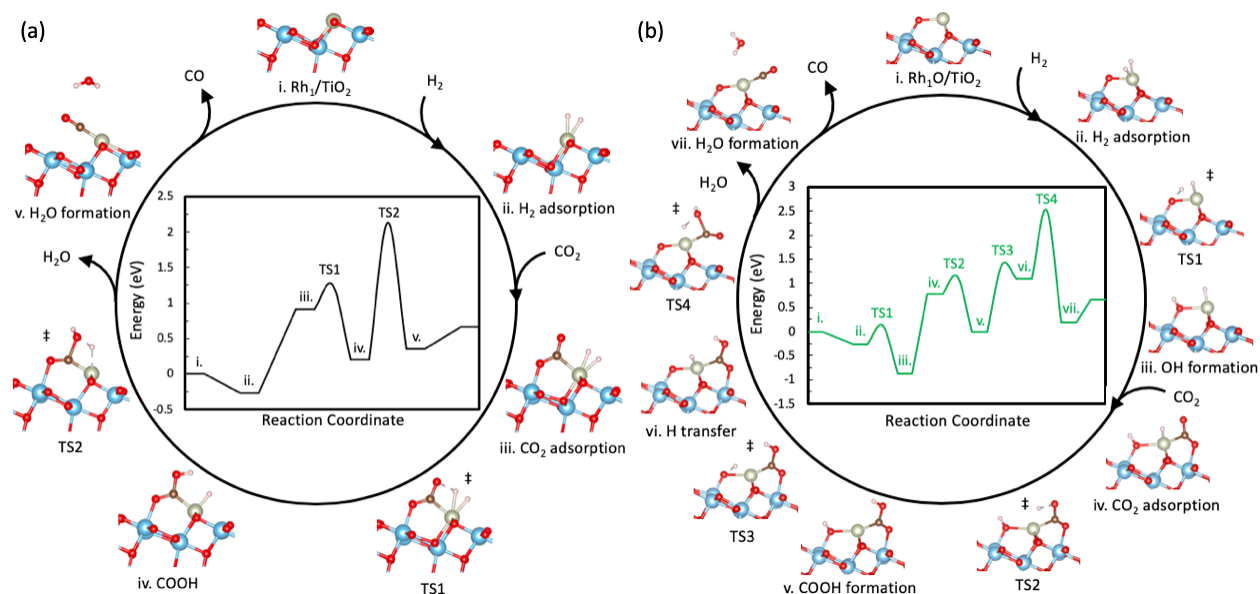


**Fig. 3.** DFT-predicted free-energy diagrams for reverse water gas shift reaction by (a)  $\text{Rh}_1/\text{TiO}_2(101)$  and (b)  $\text{Rh}_1\text{OH}/\text{TiO}_2(101)$ . Free energies were computed at 400 K and 1 atm total pressure. Atom color legend: Blue = Ti, Red = O, Gray = Rh, Brown = C, White = H.

The free energy diagrams for the rWGS mechanism of  $\text{Rh}_1/\text{TiO}_2(101)$  and  $\text{Rh}_1\text{OH}/\text{TiO}_2(101)$  are shown in **Fig. 3**. The mechanism for  $\text{Rh}_1/\text{TiO}_2(101)$  in **Fig. 3a** is the same as the proposed mechanism by Ma and colleagues,<sup>[33]</sup> with  $\text{H}_2$  and  $\text{CO}_2$  adsorbing onto  $\text{Rh}_1$ , followed by H transfer to the oxygen within  $^*\text{CO}_2$  to form  $^*\text{COOH}$ . The second hydrogen transfers to  $^*\text{COOH}$  and reacts to form  $^*\text{CO}$  and water, which is rate controlling (i.e., TS2 in **Fig. 3a**, see **Table S1** of SI for DRC analysis), where the water is weakly bound and desorbs from the surface.  $\text{CO}$  then desorbs to complete the cycle. An alternative mechanism was considered where bound  $^*\text{COOH}$  dissociates to form  $^*\text{CO}$  and  $^*\text{OH}$ , followed by  $\text{CO}$  desorption and  $^*\text{OH}$  hydrogenation to  $\text{H}_2\text{O}$  (**Fig. S3**). This mechanism was predicted to have a lower reaction rate and led to a slightly higher apparent activation barrier.

The mechanism for  $\text{Rh}_1\text{OH}/\text{TiO}_2$  in **Fig. 3b** is modeled to form a hydroxyl group next to  $\text{Rh}_1$  during the reaction that participates in  $\text{CO}_2$  hydrogenation. The starting configuration is similar to that of  $\text{Rh}_1/\text{TiO}_2(101)$ , but with an extra O atom adjacent to  $\text{Rh}_1$ .  $\text{H}_2$  adsorbs on  $\text{Rh}_1$  and dissociates onto the nearby O, forming the  $^*\text{OH}$  group and  $\text{Rh}-\text{H}$ .  $\text{CO}_2$  then adsorbs, and the H bound to  $\text{Rh}_1$  transfers to form  $^*\text{COOH}$ . The remaining H of the

$\text{OH}$  group undergoes a two-step transfer by moving to Rh and then to  $^*\text{COOH}$  to form  $^*\text{CO}$  and  $\text{H}_2\text{O}$ , which is rate controlling (TS4 in **Fig. 3b**, see **Table S1** of SI for DRC analysis).

Both mechanisms share similarities, with a stable  $^*\text{COOH}$  intermediate forming after one H transfer and a high barrier for the final H transfer to form  $\text{H}_2\text{O}$ . The activity of these two pathways is limited by the large free energy barrier to dissociate  $^*\text{COOH}$  into  $\text{CO}$  and  $\text{H}_2\text{O}$ , with  $\text{Rh}_1\text{OH}$  further stabilizing the  $^*\text{COOH}$  compared to the  $\text{Rh}_1$  without a nearby hydroxyl group. The mechanism proposed here for  $\text{Rh}_1\text{OH}$  creates a system similar to that studied by Asokan *et al.*,<sup>[32]</sup> but it does not observe the same  $\text{Rh}_1\text{OH}$  with bound  $\text{CO}$  during the reaction itself. Instead, the H from OH is used to hydrogenate  $^*\text{COOH}$  and leaves behind the O atom adjacent to  $\text{Rh}_1$ . This OH group may exist in different configurations under reaction conditions and CO-DRIFTS conditions.

The free energy diagram for the rWGS mechanism of  $\text{Rh}_1$  near  $\text{O}_{3c}\text{vac}$  is shown in **Fig. 4**. The  $\text{Rh}_1$  near  $\text{O}_{3c}\text{vac}$  mechanism begins similarly with  $\text{H}_2$  adsorption, but then  $\text{H}_2$  dissociates onto a nearby lattice oxygen ( $\text{O}_{3c}$ ). When the remaining H reacts with the lattice OH,  $\text{H}_2\text{O}$  is formed and desorbs to leave an oxygen vacancy ( $\text{O}_{3c}\text{vac}$ ), which is the step with the largest barrier (0.98 eV) and



highest DRC (see **Table S1**). CO<sub>2</sub> then adsorbs with one of its oxygen atoms in the vacancy and dissociates to form CO, thereby healing the vacancy. CO desorbs to complete the cycle, as before. Elementary steps of each studied rWGS mechanism on Rh<sub>1</sub>/TiO<sub>2</sub>, Rh<sub>1</sub>OH/TiO<sub>2</sub>, and Rh<sub>1</sub> near O<sub>3c</sub>vac are provided in the SI.

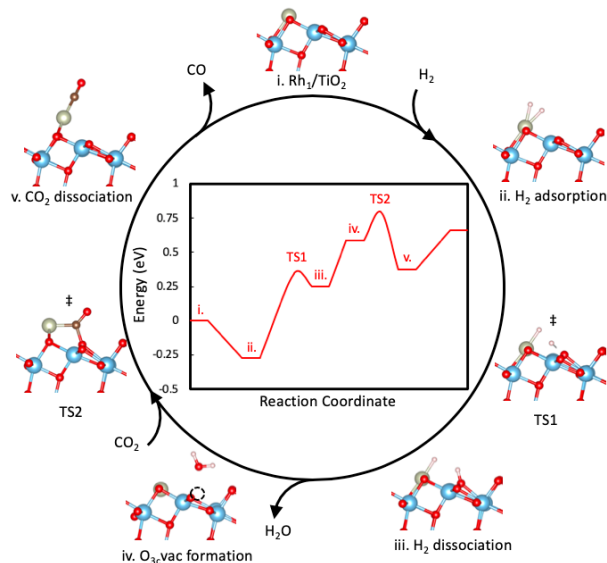


**Fig. 4.** DFT-predicted free-energy diagrams for reverse water gas shift reaction by Rh<sub>1</sub> near O<sub>3c</sub>vac, which proceeds via CO<sub>2</sub> dissociation assisted by a surface oxygen vacancy. Free energies were computed at 400 K and 1 atm total pressure. Atom color legend: Blue = Ti, Red = O, Gray = Rh, Brown = C, White = H.

The microkinetic model results in **Fig. 5a** show the Rh<sub>1</sub> near O<sub>3c</sub>vac system outperforming both the Rh<sub>1</sub> species on pristine TiO<sub>2</sub> and Rh<sub>1</sub> near a surface OH group with regards to predicted TOF. CO<sub>2</sub> reduction assisted via an oxygen vacancy has higher TOF by several orders of magnitude for the relevant temperature range of 400–600 K. Experimental observations show a TOF of 10<sup>-2.3</sup> s<sup>-1</sup> at 473 K, which is within an order of ~100 of the predicted TOF for Rh<sub>1</sub> near O<sub>3c</sub>vac but 10<sup>6</sup>–10<sup>8</sup> times too fast compared to Rh<sub>1</sub>/TiO<sub>2</sub>(101) and Rh<sub>1</sub>OH/TiO<sub>2</sub>(101). When comparing apparent activation barriers in **Fig. 5b**, the vacancy system again displays relatively close agreement with experiment. The apparent activation barriers show maxima around 500 K due to a changing degree of rate control for \*CO desorption. At higher temperature, \*CO desorption becomes more favorable, and the apparent barrier begins to decrease.

Experimentally measured apparent activation barriers range from 1.24 eV at 393–423 K (0.5 wt% Rh, gas mixture 40% H<sub>2</sub>, 10% CO<sub>2</sub>, 50% He) and 1.07 eV at 473–573 K (0.5 wt% Rh, gas mixture 24% H<sub>2</sub>, 6% CO<sub>2</sub>, 70% He).<sup>[74,75]</sup> The Rh<sub>1</sub>/TiO<sub>2</sub>(101) system has a predicted apparent barrier around 2.0–2.2 eV from 400–600 K, confirming that this previously proposed mechanism does not adequately represent the observed activity of the rWGS on Rh<sub>1</sub>/TiO<sub>2</sub>. Rh<sub>1</sub>OH/TiO<sub>2</sub>(101) likewise shares a high apparent activation barrier around 1.7–2.3 eV. In contrast, the Rh<sub>1</sub> near O<sub>3c</sub>vac system barrier is 1.3–1.7 eV within the same temperature range, in much closer agreement with experiment.

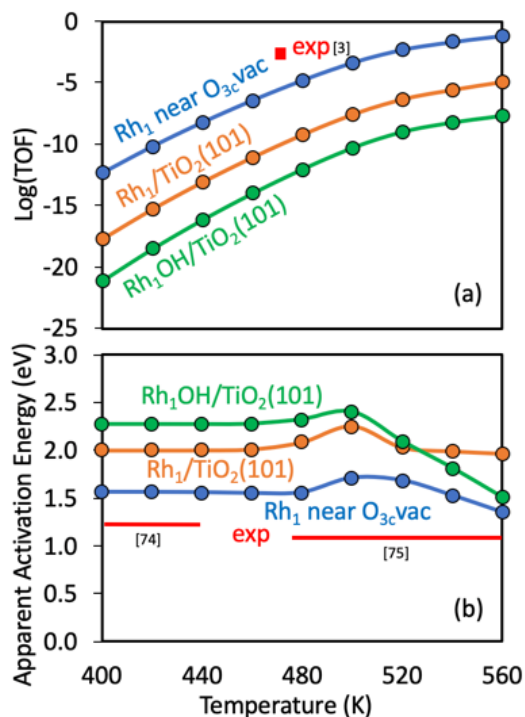


**Fig. 5.** Predicted (a) TOF vs. temperature and (b) apparent activation energy vs. temperature for Rh<sub>1</sub>/TiO<sub>2</sub>(101), Rh<sub>1</sub> near O<sub>3c</sub>vac, and Rh<sub>1</sub>OH/TiO<sub>2</sub>(101) based on mean-field microkinetic simulations. CO<sub>2</sub> and H<sub>2</sub> in a 1:4 molar ratio at a total pressure of 1 atm. Experimental data (exp) is shown inset from Ref. 3 for TOFs and Refs. 74,75 for apparent activation barriers over the denoted temperature range (solid red lines).

The Rh<sub>1</sub> through an O<sub>3c</sub>vac-assisted mechanism was predicted to have the closest agreement with experimental TOF and measured apparent activation barriers. This mechanism depends heavily on the availability of O vacancies at the surface of TiO<sub>2</sub>, which will depend on the

temperature and reducing conditions. While it is known that subsurface O vacancies are more stable than surface vacancies in anatase TiO<sub>2</sub>,<sup>[69,76]</sup> it has also been suggested that the vacancies are mobile under reaction conditions.<sup>[71]</sup> Hence, subsurface O vacancies may still play a role in the binding and dissociation of CO<sub>2</sub> by cascading diffusion of O into the lattice. The O<sub>3c</sub>vac-assisted mechanism shares similarities to what has been investigated for Rh<sub>1</sub> on rutile TiO<sub>2</sub>, with oxygen vacancies promoting the direct dissociation of CO<sub>2</sub> to CO.<sup>[59]</sup>

It is important to note that the experimental samples that we compare against typically include 25% rutile TiO<sub>2</sub>, which would offer different Rh<sub>1</sub> binding configurations and active sites, as well as a different abundance of surface oxygen vacancies. Rutile and anatase also exhibit differing amounts of electron transfer between metal and support, which in itself can reverse the observed selectivity.<sup>[77]</sup> Researchers may seek to minimize these variable support effects when studying rWGSR by using well-defined single atom binding sites such as polyoxometalates (POMs) as a model system for catalytic studies.<sup>[78]</sup>

### Effect of Nanocluster Size on rWGSR Selectivity

The catalytic activity and selectivity of nanoclusters depend on their surface composition, shape, and size.<sup>[79–81]</sup> Therefore, representative structures of nanoclusters must be known to predict its catalytic performance. Finding the stable and relevant structures of supported metal nanoclusters requires a search of the configuration space, which can be achieved via a GA structure search<sup>[52,82,83]</sup> or other methods such as stochastic surface walking,<sup>[84]</sup> basin hopping,<sup>[85,86]</sup> or replica-exchange molecular dynamics.<sup>[87]</sup> A GA is selected here for its superior performance in finding the global minima of nanoclusters compared with methods such as simulated annealing.<sup>[88]</sup> We emphasize the structures identified here are model structures. The nanoclusters may change their size and shape under reaction conditions, which is not considered in our study. The structure of a given Rh nanocluster in equilibrium with some chemical potentials of reactants could in principle be addressed using techniques such as *ab initio* Grand Canonical Monte Carlo,<sup>[83,89]</sup> albeit this approach is computationally demanding for nanoclusters and multicomponent reaction conditions.

The predicted structures of the Rh<sub>x</sub> single-atom and nanoclusters with one CO adsorbed are shown in **Fig. 6**. No major structural rearrangements occurred upon CO adsorption compared with the bare clusters (**Fig. S4**). The optimal CO adsorption configurations were found by sampling 19 different adsorption configurations distributed radially around each cluster (see SI for details). The Rh<sub>2</sub> and Rh<sub>3</sub> clusters are flat against the TiO<sub>2</sub>(101) surface with one layer of atoms, and the clusters of four atoms and above are two layers thick. In each case, the bottom layer of Rh atoms prefers to coordinate with oxygen in the TiO<sub>2</sub> lattice. Bader charge analysis of the atoms in the Rh nanocluster reveals that the atoms in the bottom layer have slight positive charge (+0.01 to +0.55 e) and the top layer atoms have slight negative charge (−0.01 to −0.11 e). Generally, the average Bader charge of the cluster decreases as size increases toward that of bulk Rh (**Fig. S5**). CO binds most strongly to the cationic Rh-Rh bridge sites at the support interface, which aligns with prior knowledge that electron donors adsorb strongly to cationic sites at metal/support interfaces.<sup>[90,91]</sup> The cationic nature of metal atoms at the nanocluster/oxide interface is a well-known phenomenon for Rh/TiO<sub>2</sub>,<sup>[33,92]</sup> and other systems such as Pt/SiO<sub>2</sub>,<sup>[93]</sup> Pt/Al<sub>2</sub>O<sub>3</sub>,<sup>[94]</sup> and Rh/faujasite.<sup>[95]</sup>

Atomically dispersed Rh<sub>1</sub> are quite cationic compared to nanoclusters (**Fig. 6**). While positive charge is typically beneficial for binding electron donors such as CO, the metal-CO binding strength has been shown to vary on a case-by-case basis due to differences in coordination geometry and the extent of  $\pi$ -back-bonding occurring.<sup>[96]</sup> In our case, CO prefers to adsorb to Rh-Rh bridge sites on Rh nanoclusters, similarly to bulk Rh, which are not present for Rh<sub>1</sub>. The presence of Rh-Rh bridge sites shows a stronger impact on CO binding than positive Bader charge alone. Weaker adsorption of CO on Rh<sub>1</sub> compared with nanoclusters should promote CO desorption before further hydrogenation to CH<sub>4</sub>. The relatively weak adsorption of CO on Rh<sub>1</sub> compared with Rh nanoclusters is quite general based on DFT studies of CO adsorption<sup>[97]</sup> and CO temperature programmed desorption experiments on systems such as Pt/TiO<sub>2</sub>,<sup>[16]</sup> Au/FeO,<sup>[98]</sup> and Rh/Al<sub>2</sub>O<sub>3</sub>.<sup>[99]</sup>

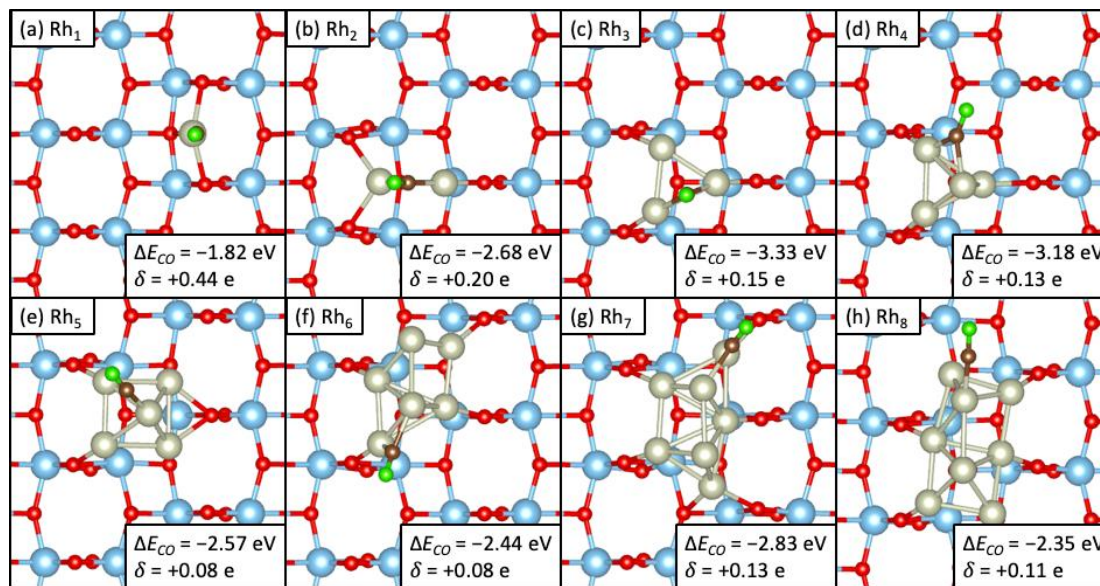


**Fig. 6.** Most stable configurations of  $Rh_x/TiO_2$  ( $x = 1-8$  atoms) with one CO adsorbed. The binding energy of CO ( $\Delta E_{CO}$ ) is given inset, as well as the average Bader charge ( $\delta$ ) of the Rh nanocluster atoms involved in the CO bond. Atom color legend: Blue = Ti, Red = O, Gray = Rh, Green = O in CO, Brown = C.

Our calculations predict that the binding energies of CO,  $CO_2$ , and  $H_2$  are all relatively weak for  $Rh_1$  compared with the larger  $Rh_x$  nanoclusters, **Fig. 7.** The adsorbate chemisorption strength increases until  $Rh_3$ , then becomes weaker as nanocluster size further increases toward bulk  $Rh(111)$ . For all cluster sizes, CO is bound more strongly than  $H_2$  and  $CO_2$ , owing to its ability to participate in  $\pi$ -back-bonding with the Rh metal.<sup>[100]</sup> Regardless, all adsorbates follow a similar trend with cluster size, where adsorbate binding is strongest for small undercoordinated clusters that can still offer two- or three-fold sites.

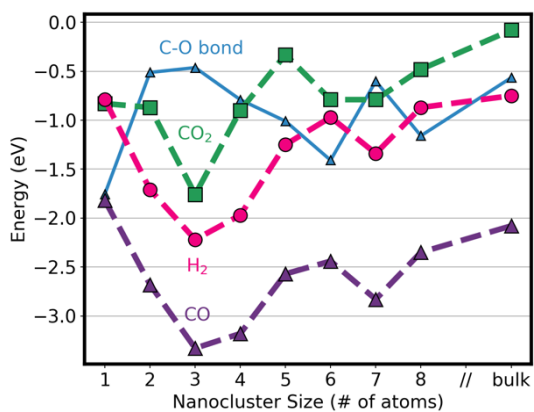


**Fig. 7.** Binding energies (dashed lines) for gaseous species of interest (CO,  $H_2$ ,  $CO_2$ ) on  $Rh_x/TiO_2$  ( $x = 1-8$  atoms). Also included is the strength of the C-O bond

(solid line) for CO bound to each  $Rh_x$  cluster. Energies for the  $Rh(111)$  bulk system are provided as the upper limit for nanocluster size. More negative energy indicates a stronger bond. Binding energies for CO correspond to geometries in Fig. 6, and those for  $CO_2$  and  $H_2$  are shown in Fig. S6 and Fig. S7.

We report a correlation between nanocluster size and the strength of the C-O bond for CO bound to each Rh nanocluster. **Fig. 7** shows that the C-O bond strength decreases from  $Rh_1$  to larger  $Rh_x$  ( $x = 2-8$ ) nanoclusters and  $Rh(111)$ . The high C-O bond strength for CO adsorbed on  $Rh_1$  compared to nanoclusters is quantitatively similar for all considered  $Rh_1$  sites (within 10% for  $Rh_1/TiO_2$ ,  $Rh_1OH/TiO_2$  and  $Rh_1$  near  $O_{3cvac}$ ). The C-O bond strength has been shown previously to be a descriptor of selectivity to CO for  $CO_2$  reduction by  $Ir_1$  species and nanoclusters.<sup>[97]</sup> For atomically dispersed catalysts such as  $Rh_1$ , in which C-O bond strength is larger than or similar to the CO binding energy, CO desorption is favored over further reduction. Because the C-O bond strength is weakened on Rh nanoclusters (including  $Rh_2$  dimers) and  $Rh(111)$  compared to  $Rh_1$  while having high CO adsorption strength, further reaction to products such as methane is favored over CO desorption. We have also investigated the CO binding and C-O bond strength trends for each



cluster when a nearby  $O_{3c}vac$  is present. The overall trends are not strongly affected by the vacancy presence (Fig. S8), indicating that the selectivity difference between  $Rh_1$  and  $Rh_x$  holds across different support conditions.

Several examples in experimental studies show the importance of CO binding energy to selectivity.<sup>[97]</sup> For a Ru/TiO<sub>2</sub> catalyst, changing the support phase from rutile to anatase resulted in an increased amount of hydrogen migrating from metal to support, known as hydrogen spillover. This hydrogen spillover is accompanied by an electron transfer from metal to support, which weakened CO binding to Ru and caused a strong selectivity shift to rWGSR.<sup>[77]</sup> A related effect has also been observed for Rh/Al<sub>2</sub>O<sub>3</sub> catalysts modified with Ni and K, where the Ni and K additives weaken the CO adsorption strength and hinder the rate of methanation.<sup>[101]</sup>

Another factor that may contribute to the increased CO<sub>2</sub>-to-CO selectivity of  $Rh_1/TiO_2$  is the lack of nearby metal sites to dissociate H<sub>2</sub>.<sup>[3]</sup> To test this hypothesis, H<sub>2</sub> dissociation on  $Rh_2$  dimers is predicted for comparison against  $Rh_1$  on defect-free TiO<sub>2</sub>(101). H<sub>2</sub> bound to  $Rh_1(CO)$  and  $Rh_2(CO)$  are chosen as starting points because the methanation reaction depends on the further hydrogenation of bound CO. It is important to consider the CO already bound to Rh, since this would impact the ability to adsorb H<sub>2</sub> and is relevant to determining selectivity between rWGSR and methanation. The activation barrier for H<sub>2</sub> dissociation is calculated for the single atom and dimer systems.

The data in Fig. 8 shows that the activation energy for H<sub>2</sub> dissociation on  $Rh_1(CO)$  is higher than that of  $Rh_2(CO)$  (0.90 vs 0.81 eV). Furthermore, H<sub>2</sub> does not adsorb nearly as strongly to  $Rh_1(CO)$  compared with  $Rh_2(CO)$  (-0.23 vs -1.09 eV), which has been hypothesized to arise from a lack of orbital overlap between  $Rh_1(CO)$  and H<sub>2</sub>.<sup>[33]</sup> The binding of H<sub>2</sub> is predicted to be weak and similar for all considered  $Rh_1$  sites (i.e.,  $Rh_1/TiO_2$ ,  $Rh_1OH/TiO_2$  and  $Rh_1$  near  $O_{3c}vac$ ). Consequently,  $Rh_1$  species cannot readily dissociate H<sub>2</sub>, in contrast to  $Rh_2$  dimers. This phenomenon is similar to how Pd-Pd sites strongly adsorb H<sub>2</sub> and accelerate dissociative H<sub>2</sub> adsorption on a Pd/Au alloy, unlike Pd-Au sites that bind H<sub>2</sub> more weakly.<sup>[102,103]</sup> These results, combined with the findings that CO adsorbs weakly and has strong C-O bond strength on  $Rh_1$  on

TiO<sub>2</sub>, explain the increased rWGSR selectivity of  $Rh_1$  compared with Rh nanoclusters. These observations may also provide insight for other atomically dispersed metal ions and nanoclusters supported on metal oxides (e.g., Ru/Al<sub>2</sub>O<sub>3</sub>,<sup>[36]</sup> Pt/CeO<sub>2</sub>,<sup>[14]</sup> Ru/CeO<sub>2</sub><sup>[15]</sup>) that display a similar rWGSR vs. methanation selectivity tradeoff for thermocatalytic CO<sub>2</sub> reduction.

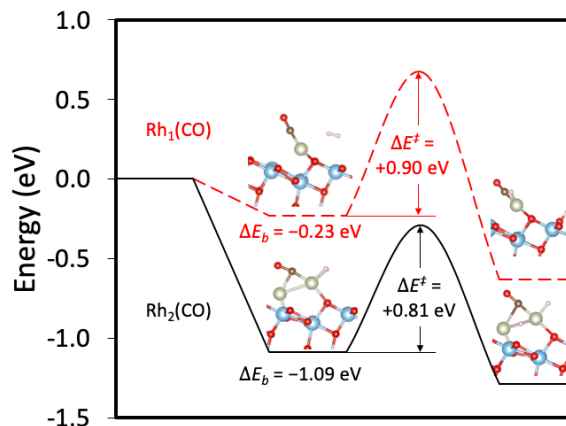


**Fig. 8.** Adsorption and dissociation of H<sub>2</sub> on  $Rh_1(CO)$  and  $Rh_2(CO)$  supported on TiO<sub>2</sub>(101). The reference state is  $Rh_1(CO)/TiO_2(101)$  or  $Rh_1(CO)/TiO_2(101)$ .  $\Delta E_b$  is the electronic binding energy of H<sub>2</sub> on  $Rh_x(CO)$  and  $\Delta E^\ddagger$  is the activation energy for hydrogen dissociation.

## CONCLUSIONS

The selectivity of thermocatalytic CO<sub>2</sub> reduction to CH<sub>4</sub> or CO depends strongly on the size of Rh species on TiO<sub>2</sub> under reducing conditions. The high CO selectivity of atomically dispersed  $Rh_1$  catalysts on anatase TiO<sub>2</sub> compared with their larger Rh nanocluster counterparts has been experimentally demonstrated, but atomistic modeling of the origin of this selectivity difference has not yet been provided. Additionally, first-principles microkinetic modeling of  $Rh_1$  active site(s) for CO<sub>2</sub> to CO reduction and the reaction pathway is lacking.

Here we computationally study plausible  $Rh_1/TiO_2$  active sites and reaction mechanisms for CO<sub>2</sub> reduction to CO. We predict that  $Rh_1$  on pristine TiO<sub>2</sub>(101) ( $Rh_1/TiO_2(101)$ ),  $Rh_1$  with a nearby hydroxyl group on TiO<sub>2</sub> ( $Rh_1OH/TiO_2(101)$ ), and  $Rh_1$  near an oxygen vacancy at a three-fold coordinated site ( $Rh_1$  near  $O_{3c}vac$ ) are likely stable  $Rh_1$  species. The relative abundance of these species will depend on the reaction conditions.<sup>[59]</sup> Among the considered  $Rh_1$

sites and reaction mechanisms, a Rh<sub>1</sub> site on TiO<sub>2</sub>(101) following CO<sub>2</sub> dissociation via an oxygen-vacancy assisted mechanism is predicted to be the most active toward CO production and had closest agreement compared with apparent activation barriers from literature.

Our findings reveal that CO adsorbs weakly and has strong C-O bond strength on Rh<sub>1</sub>/TiO<sub>2</sub> compared with larger Rh<sub>x</sub> ( $x = 2-8$  atoms) nanoclusters, including Rh<sub>2</sub> dimers. Also, Rh<sub>1</sub> has a larger activation barrier than Rh<sub>2</sub> dimers and nanoclusters to dissociate H<sub>2</sub> to reduce CO to CH<sub>4</sub> and does not have nearby Rh-metal sites to adsorb H\*. Taken together these findings rationalize the unique capability of Rh<sub>1</sub> species to selectively catalyze CO<sub>2</sub> reduction to CO compared with Rh nanoclusters.

## ASSOCIATED CONTENT

### Supporting Information

Details on: DFT modeling of formation and binding energies, genetic algorithm, Rh<sub>1</sub>/TiO<sub>2</sub> species and rWGSR reaction pathway modeling, and additional information on Rh nanocluster geometries and adsorbate binding are provided in the supporting information.

## AUTHOR INFORMATION

### Corresponding Authors

\*E-mail: bgoldsm@umich.edu

### Notes

The authors declare no competing interests.

## ACKNOWLEDGMENTS

This work was partially supported by faculty start-up funds from the University of Michigan, Ann Arbor. BRG acknowledges partial support by the U.S. Department of Energy, Office of Science, Office of Fusion Energy Sciences General Plasma Science program under Award Number DE-SC-0020232. This research used resources of the National Energy Research Scientific Computing Center (NERSC), a U.S. Department of Energy Office of Science User Facility operated under Contract No. DE-AC02-05CH11231.

## REFERENCES

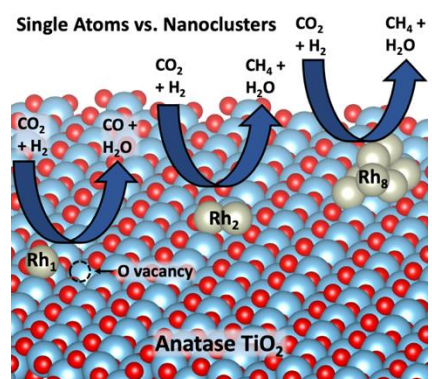
- [1] B. Qiao, A. Wang, X. Yang, L. F. Allard, Z. Jiang, Y. Cui, et al., *Nat. Chem.* **2011**, *3*, 634.
- [2] Y. Kwon, T. Y. Kim, G. Kwon, J. Yi, H. Lee, *J. Am. Chem. Soc.* **2017**, *139*, 17694.
- [3] J. C. Matsubu, V. N. Yang, P. Christopher, *J. Am. Chem. Soc.* **2015**, *137*, 3076.
- [4] M.-M. Millet, G. Algara-Siller, S. Wrabetz, A. Mazheika, F. Girgsdies, D. Teschner, et al., *J. Am. Chem. Soc.* **2019**, *141*, 2451.
- [5] X. F. Yang, A. Wang, B. Qiao, J. Li, J. Liu, T. Zhang, *Acc. Chem. Res.* **2013**, *46*, 1740.
- [6] J. Liu, *ACS Catal.* **2017**, *7*, 34.
- [7] S. C. Ammal, A. Heyden, *ACS Catal.* **2017**, *7*, 301.
- [8] S. C. Ammal, A. Heyden, *ACS Catal.* **2019**, *9*, 7721.
- [9] J. Shan, M. Li, L. F. Allard, S. Lee, M. Flytzani-Stephanopoulos, *Nature* **2017**, *551*, 605.
- [10] H. Wang, J.-X. Liu, L. F. Allard, S. Lee, J. Liu, H. Li, et al., *Nat. Commun.* **2019**, *10*, 1.
- [11] F. Doherty, H. Wang, M. Yang, B. R. Goldsmith, *Catal. Sci. Technol.* **2020**.
- [12] J. Ma, N. Sun, X. Zhang, N. Zhao, F. Xiao, W. Wei, et al., *Catal. Today* **2009**, *148*, 221.
- [13] C. Song, *Catal. Today* **2006**, *115*, 2.
- [14] Y. Wang, H. Arandiyán, J. Scott, K.-F. Aguey-Zinsou, R. Amal, *ACS Appl. Energy Mater.* **2018**, *1*, 6781.
- [15] A. Aitbekova, L. Wu, C. J. Wrasman, A. Boubnov, A. S. Hoffman, E. D. Goodman, et al., *J. Am. Chem. Soc.* **2018**, *140*, 13736.
- [16] L. DeRita, S. Dai, K. Lopez-Zepeda, N. Pham, G. W. Graham, X. Pan, et al., *J. Am. Chem. Soc.* **2017**, *139*, 14150.
- [17] J. Resasco, L. DeRita, S. Dai, J. P. Chada, M. Xu, X. Yan, et al., *J. Am. Chem. Soc.* **2020**, *142*, 169.
- [18] M. J. Hülsey, B. Zhang, Z. Ma, H. Asakura, D. A. Do, W. Chen, et al., *Nat. Commun.* **2019**, *10*, 1330.
- [19] C. Wang, X.-K. Gu, H. Yan, Y. Lin, J. Li, D. Liu, et al., *ACS Catal.* **2017**, *7*, 887.
- [20] H. Yan, H. Cheng, H. Yi, Y. Lin, T. Yao, C. Wang, et al., *J. Am. Chem. Soc.* **2015**, *137*, 10484.
- [21] M. A. Newton, C. Belder-Coldeira, A. Martínez-Arias, M. Fernández-García, *Nat. Mater.* **2007**, *6*, 528.



- [22] A. J. Dent, J. Evans, S. G. Fiddy, B. Jyoti, M. A. Newton, M. Tromp, *Angew. Chem. Int. Ed.* **2007**, *46*, 5356.
- [23] A. Berkó, J. Szökő, F. Solymosi, *Surf. Sci.* **2004**, *566–568*, 337.
- [24] F. Solymosi, M. Pasztor, *J. Phys. Chem.* **1985**, *89*, 4789.
- [25] Takanori. Mizushima, Kazuyuki. Tohji, Yasuo. Udagawa, Akifumi. Ueno, *J. Phys. Chem.* **1990**, *94*, 4980.
- [26] B. R. Goldsmith, E. D. Sanderson, R. Ouyang, W. X. Li, *J. Phys. Chem. C* **2014**, *118*, 9588.
- [27] R. Ouyang, J.-X. Liu, W.-X. Li, *J. Am. Chem. Soc.* **2013**, *135*, 1760.
- [28] A. Berkó, F. Solymosi, *J. Catal.* **1999**, *183*, 91.
- [29] J. Evans, B. Hayden, F. Mosselmans, A. Murray, *Surf. Sci.* **1994**, *301*, 61.
- [30] J. Evans, B. Hayden, F. Mosselmans, A. Murray, *Surf. Sci. Lett.* **1992**, *279*, L159.
- [31] M. Frank, R. Kühnemuth, M. Bäumer, H.-J. Freund, *Surf. Sci.* **1999**, *427–428*, 288.
- [32] C. Asokan, H. V. Thang, G. Pacchioni, P. Christopher, *Catal. Sci. Technol.* **2020**, *10*, 1597.
- [33] S. Ma, W. Song, B. Liu, H. Zheng, J. Deng, W. Zhong, et al., *Catal Sci Technol* **2016**, *6*, 6128.
- [34] I. V. Chernyshova, P. Somasundaran, S. Ponnurangam, *Proc. Natl. Acad. Sci.* **2018**, *115*, E9261.
- [35] O. R. Luca, A. Q. Fenwick, *J. Photochem. Photobiol. B* **2015**, *152*, 26.
- [36] J. H. Kwak, L. Kovarik, J. Szanyi, *ACS Catal.* **2013**, *3*, 2449.
- [37] J. Lin, A. Wang, B. Qiao, X. Liu, X. Yang, X. Wang, et al., *J Am Chem Soc* **2013**, *135*, 15314.
- [38] G. Kresse, J. Hafner, *Phys. Rev. B* **1993**, *47*, 558.
- [39] G. Kresse, J. Furthmüller, *Comput. Mater. Sci.* **1996**, *6*, 15.
- [40] G. Kresse, J. Furthmüller, *Phys. Rev. B* **1996**, *54*, 11169.
- [41] G. Kresse, D. Joubert, *Phys. Rev. B* **1999**, *59*, 11.
- [42] M. R. Ranade, A. Navrotsky, H. Z. Zhang, J. F. Banfield, S. H. Elder, A. Zaban, et al., *Proc. Natl. Acad. Sci.* **2002**, *99*, 6476.
- [43] A. Vittadini, M. Casarin, A. Selloni, *Theor. Chem. Acc.* **2007**, *117*, 663.
- [44] R. Hengerer, B. Bolliger, M. Erbudak, M. Grätzel, *Surf. Sci.* **2000**, *460*, 162.
- [45] A. H. Larsen, J. Jens, J. Blomqvist, *J. Phys. Condens. Matter* **2017**, *29*, 273002.
- [46] L. Iyengar, K. V. K. Rao, S. V. N. Naidu, *J. Am. Ceram. Soc.* **1969**, *53*, 124.
- [47] G. Henkelman, B. P. Uberuaga, H. Jónsson, *J. Chem. Phys.* **2000**, *113*, 9901.
- [48] S. Grimme, J. Antony, S. Ehrlich, H. Krieg, *J. Chem. Phys.* **2010**, *132*.
- [49] B. J. Morgan, G. W. Watson, *Surf. Sci.* **2007**, *601*, 5034.
- [50] Z. Hu, H. Metiu, *J. Phys. Chem. C* **2011**, *115*, 5841.
- [51] N. Mina-Camilde, C. Manzanares I., J. F. Caballero, *J. Chem. Educ.* **1996**, *73*, 804.
- [52] L. B. Vilhelmsen, B. Hammer, *J. Chem. Phys.* **2014**, *141*, 044711.
- [53] S. R. Bahn, K. W. Jacobsen, *Comput. Sci. Eng.* **2002**, *4*, 56.
- [54] A. Bruix, J. T. Margraf, M. Andersen, K. Reuter, *Nat. Catal.* **2019**, *2*, 659.
- [55] C. T. Campbell, *ACS Catal.* **2017**, *7*, 2770.
- [56] I. A. W. Filot, R. J. P. Broos, J. P. M. van Rijn, G. J. H. A. van Heugten, R. A. van Santen, E. J. M. Hensen, *ACS Catal.* **2015**, *5*, 5453.
- [57] J.-X. Liu, D. Richards, N. Singh, B. R. Goldsmith, *ACS Catal.* **2019**, *9*, 7052.
- [58] M. D. Porosoff, B. Yan, J. G. Chen, *Energy Environ. Sci.* **2016**, *9*, 62.
- [59] Y. Tang, C. Asokan, M. Xu, G. W. Graham, X. Pan, P. Christopher, et al., *Nat. Commun.* **2019**, *10*, 1.
- [60] J. T. Yates, T. M. Duncan, R. W. Vaughan, *J Chem Phys* **1979**, *71*, 9.
- [61] J. T. Yates, T. M. Duncan, S. D. Worley, R. W. Vaughan, *J. Chem. Phys.* **1979**, *70*, 1219.
- [62] H. Miessner, I. Burkhardt, D. Gutschick, A. Zecchina, C. Morterra, G. Spoto, *J. Chem. Soc. Faraday Trans. 1 Phys. Chem. Condens. Phases* **1989**, *85*, 2113.
- [63] S. Trautmann, M. Baerns, *J. Catal.* **1994**, *150*, 335.
- [64] J. Rasko, F. Solymosi, *J. Phys. Chem.* **1994**, *98*, 7147.
- [65] M. Frank, R. Kühnemuth, M. Bäumer, H.-J. Freund, *Surf. Sci.* **2000**, *454–456*, 968.

- [66] Y. Ji, Y. Luo, *J. Am. Chem. Soc.* **2016**, *138*, 15896.
- [67] É. Novák, K. Fodor, T. Szailer, A. Oszkó, A. Erdöhelyi, *Top. Catal.* **2002**, *20*, 107.
- [68] X. Pan, M.-Q. Yang, X. Fu, N. Zhang, Y.-J. Xu, *Nanoscale* **2013**, *5*, 3601.
- [69] Y. He, O. Dulub, H. Cheng, A. Selloni, U. Diebold, *Phys. Rev. Lett.* **2009**, *102*, 106105.
- [70] H. Guan, J. Lin, B. Qiao, S. Miao, A.-Q. Wang, X. Wang, et al., *AIChE J.* **2017**, *63*, 2081.
- [71] P. Scheiber, M. Fidler, O. Dulub, M. Schmid, U. Diebold, W. Hou, et al., *Phys. Rev. Lett.* **2012**, *109*, 136103.
- [72] M. Setvín, U. Aschauer, P. Scheiber, Y.-F. Li, W. Hou, M. Schmid, et al., *Science* **2013**, *341*, 988.
- [73] S. Kattel, B. Yan, J. G. Chen, P. Liu, *J. Catal.* **2016**, *343*, 115.
- [74] A. Karelovic, P. Ruiz, *J. Catal.* **2013**, *301*, 141.
- [75] Z. L. Zhang, A. Kladi, X. E. Verykios, *J. Catal.* **1994**, *148*, 737.
- [76] H. Cheng, A. Selloni, *Phys. Rev. B* **2009**, *79*, 092101.
- [77] X. Li, J. Lin, L. Li, Y. Huang, X. Pan, S. E. Collins, et al., *Angew. Chem. Int. Ed.* **2020**, *59*, 19983.
- [78] M. J. Hülsey, G. Sun, P. Sautet, N. Yan, *Angew. Chem. Int. Ed.* **2021**, *60*, 4764.
- [79] H. Zhai, A. N. Alexandrova, *ACS Catal.* **2017**, *7*, 1905.
- [80] A. Sanchez, S. Abbet, U. Heiz, W.-D. Schneider, H. Häkkinen, R. N. Barnett, et al., *J. Phys. Chem. A* **1999**, *103*, 9573.
- [81] A. T. Bell, *Science* **2003**, *299*, 1688.
- [82] P. C. Jennings, S. Lysgaard, J. S. Hummelshøj, T. Vegge, T. Bligaard, *Npj Comput. Mater.* **2019**, *5*, 46.
- [83] J.-X. Liu, Y. Su, I. A. W. Filot, E. J. M. Hensen, *J. Am. Chem. Soc.* **2018**, *140*, 4580.
- [84] C. Shang, Z.-P. Liu, *J. Chem. Theory Comput.* **2013**, *9*, 1838.
- [85] D. J. Wales, J. P. K. Doye, *J. Phys. Chem. A* **1997**, *101*, 5111.
- [86] G. G. Rondina, J. L. F. Da Silva, *J. Chem. Inf. Model.* **2013**, *53*, 2282.
- [87] Y. Sugita, Y. Okamoto, *Chem. Phys. Lett.* **1999**, *314*, 141.
- [88] D. M. Deaven, K. M. Ho, *Phys. Rev. Lett.* **1995**, *75*, 288.
- [89] R. B. Wexler, T. Qiu, A. M. Rappe, *J. Phys. Chem. C* **2019**, *123*, 2321.
- [90] W. T. Wallace, R. L. Whetten, *J. Phys. Chem. B* **2000**, *104*, 10964.
- [91] S. Kattel, P. Liu, J. G. Chen, *J. Am. Chem. Soc.* **2017**, *139*, 9739.
- [92] C.-T. Yang, B. C. Wood, V. R. Bhethanabotla, B. Joseph, *J. Phys. Chem. C* **2014**, *118*, 26236.
- [93] C. S. Ewing, M. J. Hartmann, K. R. Martin, A. M. Musto, S. J. Padinjarekutt, E. M. Weiss, et al., *J. Phys. Chem. C* **2015**, *119*, 2503.
- [94] A. Beniya, S. Higashi, N. Ohba, R. Jinnouchi, H. Hirata, Y. Watanabe, *Nat. Commun.* **2020**, *11*, 1.
- [95] G. N. Vayssilov, B. C. Gates, N. Rösch, *Angew. Chem. Int. Ed.* **2003**, *42*, 1391.
- [96] Z. Jakub, J. Hulva, M. Meier, R. Bliem, F. Kraushofer, M. Setvin, et al., *Angew. Chem.* **2019**, *131*, 14099.
- [97] X. Chen, X. Su, H.-Y. Su, X. Liu, S. Miao, Y. Zhao, et al., *ACS Catal.* **2017**, *7*, 4613.
- [98] Sh. K. Shaikhutdinov, R. Meyer, M. Naschitzki, M. Bäumer, H.-J. Freund, *Catal. Lett.* **2003**, *86*, 211.
- [99] D. N. Belton, S. J. Schmieg, *Surf. Sci.* **1988**, *202*, 238.
- [100] G. Blyholder, *J. Phys. Chem.* **1964**, *68*, 2772.
- [101] D. Heyl, U. Rodemerck, U. Bentrup, *ACS Catal.* **2016**, *6*, 6275.
- [102] W.-Y. Yu, G. M. Mullen, C. B. Mullins, *J. Phys. Chem. C* **2013**, *117*, 19535.
- [103] F. R. Lucci, M. T. Darby, M. F. G. Mattered, C. J. Ivimey, A. J. Therrien, A. Michaelides, et al., *J. Phys. Chem. Lett.* **2016**, *7*, 480.

## Table of Contents Entry



The thermocatalytic reduction of CO<sub>2</sub> + H<sub>2</sub> by Rh/TiO<sub>2</sub> proceeds via two competing reaction mechanisms depending on whether single atoms or nanoclusters are used. DFT and microkinetic modeling suggest a preferred reaction involving CO<sub>2</sub> dissociation assisted by a support oxygen vacancy. Rh<sub>1</sub> sites are selective toward CO rather than CH<sub>4</sub> because of the weak adsorption of CO, large barrier for C-O bond dissociation, and the lack of nearby metal sites for H<sub>2</sub> dissociation, in contrast to Rh<sub>x</sub> nanoclusters, including Rh<sub>2</sub> dimers.